Biomedical Signal Processing and Control 119 (2026) 109840

Contents lists available at ScienceDirect

Biomedical Signal Processing and Control

journal homepage: www.elsevier.com/locate/bspc

PulseAI: An automated machine learning-based augmentation index detector for arterial stiffness monitoring from cuff-based measurements

Alessio Tamborini [a,*], Arian Aghilinejad [b], Morteza Gharib [a]

[a] Department of Medical Engineering, California Institute of Technology, USA
[b] Department of Bioengineering, University of California, Merced, USA

ARTICLE INFO

Keywords:
Blood pressure
Pulse Waveform Analysis
Machine learning
Augmentation index
Arterial stiffness
Brachial cuff

ABSTRACT

Arterial stiffness is a fundamental characteristic of circulatory physiology and a well-established predictor of cardiovascular risk and mortality. However, routine clinical assessment remains limited by the need for dual-site measurements. To address this challenge, we developed a machine learning algorithm – PulseAI – for automated fiducial point detection on brachial cuff waveforms for single-site assessment of arterial stiffness. PulseAI was trained and evaluated using a clinical dataset comprising 5,215 waveforms from 145 heterogeneous subjects. Performance was assessed on fiducial point predictions accuracy (inflection point, t_i, and dicrotic notch, t_n) and downstream pulse waveform analysis (PWA) metrics. Our multi-channel convolutional neural network (PulseAI) reported a median [IQR] on mean absolute error for fiducial point detection of 5 [3, 10] ms. PulseAI demonstrated high accuracy in predicting t_i ($r = 0.913$, $p < 0.0001$) and t_n ($r = 0.939$, $p < 0.0001$), with an average prediction error of 12.6 ms and 6.2 ms for t_i and t_n, respectively. While the t_n results are comparable to other academic models reporting ~10 ms errors, our approach provides both fiducial point indices from a single model. PWA features derived from PulseAI closely matched those derived from human-annotated labels, including systolic pressure–time integral ($r = 0.988$, $p < 0.0001$), augmentation index (AIx) ($r = 0.990$, $p < 0.0001$), and end systolic pressure ($r = 0.998$, $p < 0.0001$). AIx tertiles showed statistically significant association with height-adjusted pulse transit time ($p < 0.05$), used as a surrogate of arterial stiffness, demonstrating the model's sensitivity to stiffness-related changes. These findings demonstrate that PulseAI enables accurate fiducial point detection and represents a clinically viable tool for automated, single-site monitoring of arterial stiffness.

1. Introduction

Despite significant advances in cardiovascular care, cardiovascular disease (CVD) remains the leading cause of mortality in developed countries [1]. While blood pressure (BP) is a well-established risk factor, additional markers have been shown to play a critical role in the development and progression of CVD [2–4]. Among these, arterial stiffness has emerged as an independent predictor of cardiovascular risk and mortality [5,6]. Large artery elasticity is a fundamental characteristic of circulatory physiology, helping to buffer the pulsatile flow generated by cardiac ejection during systole [7]. Pulse wave velocity (PWV) is a widely recognized metric for assessing arterial stiffness, calculated using the pulse transit time (PTT) and the propagation distance between two measurement sites [8]. While PWV is considered the gold standard for arterial stiffness assessment, its reliance on dual-site measurement introduces practical challenges in clinical settings [9]. On one hand, efforts have been made to estimate PWV from single-point measurements using machine learning models, offering a potentially simpler alternative. Jin et al. developed a Gaussian Process Regression method to estimate PWV from selected waveform features [10]. Mitchell et al., using a deep learning approach, trained a convolutional neural network (CNN) to predict carotid-to-femoral PWV from single, uncalibrated waveforms acquired at the radial, brachial, or femoral sites [11]. Beyond these direct applications, machine learning is being widely adopted in cardiology for tasks including cardiovascular risk stratification, transfer functions, and medical image analysis, demonstrating its broad utility [12–15]. On the other hand, surrogate parameters have been investigated for this purpose. Augmentation index (AIx) has gained attention as a measure of systemic arterial stiffness derived from a single cardiac waveform measurement [16]. However, the clinical utility of such parameters is dependent not only on their theoretical significance but also on the reliability and precision of their measurement [16–18].

* Corresponding author.
E-mail address: atambori@caltech.edu (A. Tamborini).

https://doi.org/10.1016/j.bspc.2026.109840
Received 22 April 2025; Received in revised form 26 January 2026; Accepted 9 February 2026
Available online 14 February 2026

The first key factor influencing this accuracy is the reliability of pulse waveform acquisition. Increasing attention has been directed toward noninvasive systems such as brachial cuff devices, due to their ease of use and improved measurement repeatability—both essential for clinical adoption [19,20]. In this context, suprasystolic blood pressure (sSBP) measurements mode have gained prominence for its ability to capture detailed and feature rich pressure waveforms [14,15,19,21–24]. Beyond waveform acquisition, the accurate identification of fiducial points along the cardiac pressure waveform remains a critical challenge. These points correspond to key physiological events, such as the arrival of the reflected wave and the closure of the aortic valve, typically marked by the inflection point and the dicrotic notch, respectively. However, their morphology can vary significantly depending on the population and study characteristics. For instance, the dicrotic notch may appear as a distinct physical notch or a subtle incisura, while the inflection point can occur either before or after the systolic peak. This variability complicates the development of universally applicable mathematical rules for their detection, often leading researchers to rely on manual identification or study-specific criteria. For example, Sugawara et al. used the fourth order derivative to find the systolic inflection point [25,26], Munir et al. used the first order derivatives and tangents to determine the location of the inflection point [27], and Ueda et al. used an experienced observed to measure the inflection point [28]. To this end, several efforts have been dedicated towards developing algorithmic approaches for automatic identification. Saffarpour et al. developed Physiowise, a physics-aware approach to dicrotic notch identification [29], Pal et al. pioneered an iterative envelope mean method for detection of the dicrotic notch [30,31], and Hoeksel et al. uses a three-element windkessel model to estimate flow from pressure and then identify the dicrotic notch [32]. While these methods showed promising results, they only focused on a single identification task and therefore require complementation with other methods for full detection. With the substantial increment of healthcare dataset size, there is a growing need for comprehensive, high-precision, and automated tools to facilitate and standardize this process.

In this study, we assess the accuracy and generalizability of machine learning for fiducial point detection, specifically identifying the inflection point and the dicrotic notch, using our model, PulseAI. We train and evaluate the model on a dataset of manually labeled and human-annotated cardiac pressure waveforms acquired from a brachial cuff system operating in sSBP mode [33]. To benchmark its performance, we compare PulseAI's results against conventional mathematical methods described in the literature and use the 30 ms reported error ranges as an acceptance criteria [29,30]. To demonstrate the physiological relevance of our machine learning pipeline, we have also examined the association between arterial stiffness and AIx derived from our proposed algorithm. Lastly, in order to provide a standardized and accessible platform for researchers to integrate into their own studies, the optimized trained model of this study has been made publicly available on GitHub.

2. Methods

2.1. Clinical study design

Brachial pressure waveforms were recorded using a custom and laboratory-developed investigational brachial cuff device designed for high-resolution waveform acquisition [33]. The device has been previously validated against intra-arterial measurements for waveform accuracy [21]. The device's protocol first performed an oscillometric blood pressure measurement for calibration, followed by pulse waveform capture using the inflate-and-hold methodology. This methodology was applied at the sSBP hold, defined as 35 mmHg above the systolic blood pressure (SBP), and maintained for 40 s.

The dataset analyzed in this study consists of brachial pressure waveforms collected during cardiac catheterization procedures. Measurements were performed with subjects in the supine position, and the brachial cuff was placed on the left arm following standard cuff placement guidelines. The study enrolled individuals aged 21 years or older who were referred for non-emergent left heart catheterization between September 2021 and September 2022. Exclusion criteria included recent severe cardiac events (within one week), inability to undergo routine blood pressure measurement, and contraindications to catheterization. Simultaneous aortic catheterization waveforms were recorded during brachial cuff measurements to enable PTT calculations. The signals were captured at a sampling rate of 1 kHz.

The study was approved by the Institutional Review Board of Western and Salus. Written informed consent was obtained from all participants before the procedure. The study adhered to the principles of the Declaration of Helsinki.

2.2. Study population

The study population included 145 subjects with a mean age of 66 ± 9 years, 88 males (61%), and a mean body mass index (BMI) of 29.0 ± 5.5 kg/m^2. Patient characteristics for the entire study population are summarized in Table 1. The analysis generated a dataset of 5215 waveforms from the brachial cuff during the sSBP hold phase. The distribution of cardiac cycles per individual showed a median of 37, with interquartile ranges of [31,34] cycles per subject, a maximum of 62, and a minimum of 2 (Fig. S2). The study population was partitioned into three cohorts at the subject level using a 70%-10%-20% train-validation-test split, resulting in cohorts of 102, 14, and 29 subjects, and 3646, 515, and 1054 waveforms, respectively (Fig. 1B). Table S2 provides a summary of the population characteristics for the training, validation, and test cohorts. Fig. S3 shows the cumulative distribution function of the fiducial points in the time-based format as well as the unit-normalized configuration; the train-validation-test cohorts showed overlapping distributions for both $\widetilde{t}_i$ and $\widetilde{t}_n$.

2.3. Data and signal preprocessing

The brachial cuff recordings were manually inspected to remove instances of apparatus malfunction, procedural errors, saturated sensor output, and arrhythmias. The sSBP pressure signal recordings from the brachial cuff were segmented into individual cardiac cycles using the foot-to-foot partition method [8]. Each cardiac cycle can be represented mathematically as,

$$p_m = p(t_m), m = 0, 1, \cdots, N-1. \quad (1)$$

where N is the length of the cardiac cycle. This segmentation resulted in a dataset containing multiple cardiac cycles for each subject, with each cycle treated as a unique but dependent data point. While cycles from the same subject were considered distinct, they were not independent due to the shared underlying physiological characteristics. Fiducial points of interest on the pressure waveform – namely the peak pressure, inflection point and dicrotic notch – were manually identified for the entire dataset:

Table 1
Study population characteristics.

Variable	Quantity (n = 145)
Age, years	66 ± 9
Height, cm	170 ± 10
Weight, kg	84.6 ± 19.2
BMI, kg/m^2	29.0 ± 5.5
Male, n (%)	88 (61%)
White, n (%)	96 (66%)
Smoker, n (%)	22 (15%)
Diabetes, n (%)	51 (35%)
Hypertension, n (%)	115 (79%)
Hyperlipidemia, n (%)	107 (74%)

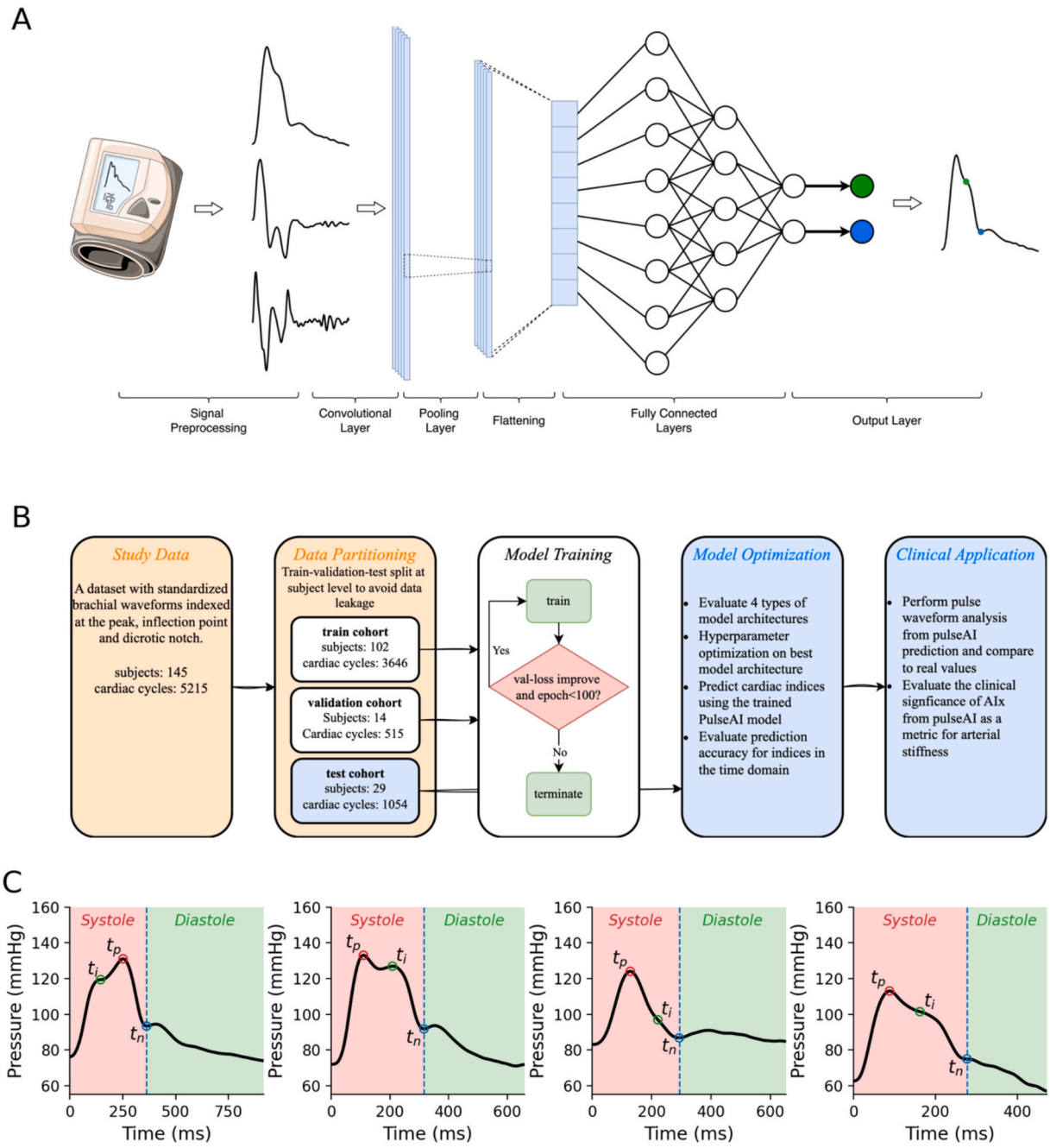

Fig. 1. Overview of the PulseAI method for fiducial point detection. (A) Conceptual overview of the PulseAI algorithm, including procedural steps and data flow. (B) Schematic representation of the study design and data utilization workflow. (C) Brachial pressure waveform with labeled fiducial points: peak time (t_p), inflection point time (t_i), and dicrotic notch time (t_n). Shaded regions indicate the systolic and diastolic phases of the cardiac cycle.

t_p = *time of peak pressure*

t_i = *time of inflection point*

t_n = *time of dicrotic notch*

These fiducial points represent key pressure waveform features: peak time corresponds to maximal systolic pressure, the inflection time marks the arrival of the reflected wave, and the dicrotic notch time indicates the closure of the aortic valve. The cardiac cycles along with the fiducial points were combined to generate the dataset for the study.

Both dataset components – fiducial points and brachial cuff waveforms – were preprocessed before being fed into the machine learning portion of the study. The fiducial points were converted to unit-normalized quantities by dividing for the duration of the cardiac cycle, denoted T, as shown below:

$$\widetilde{t_p} = \frac{t_p}{T}; \widetilde{t_i} = \frac{t_i}{T}; \widetilde{t_n} = \frac{t_n}{T} \tag{2}$$

This normalization ensures that the fiducial points all lie within the range 0 to 1, which is optimal for an ML model output.

Brachial cuff waveforms were individually resampled to a fixed length of 1000 samples to ensure consistent input size to the ML model. Resampling was performed using a Fourier-based methodology along the time axis, which is outlined in Algorithm 1. Resampled waveforms were standardized to a mean value of zero and a standard deviation of one. Upon performing both procedures, we define these as resampled and normalized waveforms. The first and second derivatives were

computed using the finite difference method on the resampled and normalized waveforms; interior points were computed with second-order accurate central differences while at the boundaries we used one-sided differences to preserve signal length. This signal preprocessing generated a dataset of waveforms – signal, first derivative and second derivative – with fixed length, centered around zero, and a standard deviation of one.

Algorithm 1: Fourier-based Resampling Method

Input: waveform signal $p(t)$, desired signal length M
Output: resampled signal $p'(t)$
1. **Discrete Fourier Transform**
Convert signal from time domain to frequency domain:
$P_k = \sum_{m=0}^{N-1} p_m e^{-\frac{j2\pi km}{N}}, k = 0,1,\cdots,N-1$
where P_k are the frequency components of the original signal, and N is the length of the original signal
2. **Frequency Domain Resampling**
If M > N, apply zero-padding to the frequency components:
$$P'_k = \begin{cases} P_k, k = 0,\cdots,N/2 \\ 0, N/2 < k < M - N/2 \\ P_k, k = M - N/2,\cdots,M-1 \end{cases}$$
If M < N, truncate the frequency components:
$P'_k = P_k, k = 0,1,\cdots,M-1.$
3. **Inverse Discrete Fourier Transform**
Convert the signal back to the time domain:
$p'_j = \frac{1}{M}\sum_{k=0}^{M-1} P'_k e^{-\frac{j\pi kj}{M}}, j = 0,1,\cdots,M-1.$

The dataset was partitioned for standard model training and testing using a 70%-10%-20% train-validation-test split ratio. Given the dependence of cardiac cycles within a given subject, the split was performed at the subject level rather than the cardiac cycle level to prevent data leakage. The training cohort was used for model training, the validation cohort for early stopping during training, and the testing cohort for model evaluation.

2.4. PulseAI method

The PulseAI method is a machine learning approach developed to identify fiducial points on the cardiovascular pressure waveform. The model takes as input a single cardiac cycle and outputs the unit-normalized indices of the fiducial points. In this model implementation, the PulseAI method was trained to predict the relative time position of the inflection point and the dicrotic notch for the brachial pressure waveforms in the sSBP hold. Fig. 1a shows an overview of the multi-channel CNN (mcCNN) model implemented for PulseAI. The PulseAI method was optimized for predicting the fiducial points t_i and t_n through a two-stage process: model architecture evaluation and hyperparameter tuning. Fig. S1 in the supplementary material provides an overview of the optimization approach used in this study.

In the first stage, we evaluated four model architectures: a CNN, a mcCNN, a multilayer perceptron (MLP), and a Fourier-based Neural Network (fNN). At this stage, all models used an element-wise mean-square error loss function.

The CNN model consisted of three convolutional blocks, each sequentially comprising a 1D convolutional layer, ReLU activation, and max pooling. The convolutional layers had 8, 16, and 16 filters, respectively, with a kernel size of 3, a stride of 1, and padding of 1. One-dimensional max-pooling with a kernel size of 2 and a stride of 2 was applied after each block to progressively downsample the feature maps. The output of the final convolutional block was flattened and passed through two fully connected layers: the first with 128 units and the second mapping to the two output classes. The model processed a single-channel input, representing the resampled and normalized waveform of length 1000. The mcCNN model had the same architecture as the CNN model but processed three input channels: the resampled and normalized waveform, its first derivative, and its second derivative, each of length 1000. The use of derivatives was intended to capture high-frequency features embedded within the signal shape.

The MLP model consisted of four fully connected layers, mapping an input of 1000 units to two output units. The three hidden layers contained 128, 64, and 32 units, respectively, each followed by a ReLU activation function and a dropout rate of 0.35. The fNN model was a fully connected feedforward neural network operating in the frequency domain. The input signal was first transformed into the frequency domain, truncated to retain a limited number of modes, then flattened into its real and imaginary components before being passed into the network. The network architecture beyond this preprocessing step was identical to the MLP model. The model architecture that yielded the best performance was selected for hyperparameter optimization.

The hyperparameter tuning phase focused on three key factors: loss function selection, data augmentation, and regularization. First, we compared model performance with different base loss functions: mean squared error (MSE), mean absolute error (MAE), and Huber loss with $\delta = 10$ ms. A penalty term is added to each base loss function making the total loss:

$$\mathscr{L}_{total} = \mathscr{L}_{base} + \mathscr{L}_{penalty} \tag{3}$$

The penalty term computes the average of all positive index differences between the inflection point and dicrotic notch. This penalty effectively enforces the physiological constraint that the inflection point occurs before the dicrotic notch.

$$\mathscr{L}_{penalty} = \frac{1}{n}\sum_{i=1}^{n} \max\left(0, \widehat{Y}_{i,0} - \widehat{Y}_{i,1}\right) \tag{4}$$

where $i \in \{1,\cdots,n\}$ indexes the samples within the dataset.

Next, we investigated the impact of data augmentation, generating additional training signals by applying truncation and resampling, and scaling. Three augmentation strategies were evaluated: (1) truncation and resampling, (2) scaling, and (3) both applied sequentially. Finally, we explored regularization techniques, testing dropout, weight decay, and their combined effect. At each step, the best-performing model configuration was carried forward for further evaluation. This tuning process resulted in nine experimental scenarios, detailed in Table S1 in the supplementary material. Fig. S1 summarizes model selection and hyperparameter tuning.

2.5. Empirical method

The empirical method served as a reference for comparing model performance in identifying fiducial points along the pressure waveform. This approach was used to detect both the inflection point, t_i, as well as the dicrotic notch, t_n. The inflection point was determined using the fourth-order derivative, following the guidelines established by Takazawa et al. [35]. The dicrotic notch was identified as the first peak of the second derivative occurring after the minimum of the first derivative, as described by Peter et al. [36] and Takazawa et al. [37]. The mathematical steps behind the empirical method have been summarized in Algorithm 2.

Algorithm 2: Empirical Method for Calculating Fiducial Points

Input: waveform signal
Output: t_p, t_i, t_n (fiducial point indices)
1. **Compute Derivatives:**
1.1. $p(t)_{d1} \leftarrow \nabla p(t)$ (first derivative)
1.2. $p(t)_{d2} \leftarrow \nabla p(t)_{d2}$ (second derivative)
1.3. $p(t)_{d3} \leftarrow \nabla p(t)_{d2}$ (third derivative)
1.4. $p(t)_{d4} \leftarrow \nabla p(t)_{d3}$ (fourth derivative)
2. **Identify Maximum Value**:
2.1. $t_p \leftarrow \text{argmax}(p(t))$
3. **Determine Slope at Maximum**:
3.1. $slope_{d4} \leftarrow p(t_{max})_{d4}$
4. **Identify Inflection Point**:
If $slope_{d4} > 0$ (late systolic peak):
4.1. Identify zero-crossings of $p(t)_{d4}$ (positive to negative)

(*continued on next page*)

(*continued*)

Algorithm 2: Empirical Method for Calculating Fiducial Points

If at least two zero-crossings exist before t_p:
  $t_i \leftarrow$ second zero-crossing of $p(t)_{d4}$
Else:
  $t_i \leftarrow$None
Else (early systolic peak):
  4.2. Identify zero-crossings of $p(t)_{d4}$ (negative to positive)
  If at least three zero-crossings exist after t_p:
    $t_i \leftarrow$ third zero-crossing of $p(t)_{d4}$
  Else:
    $t_i \leftarrow$None
5. **Identify Dicrotic Notch**:
  5.1. $t_{d1,min} \leftarrow \text{argmin}(p(t)_{d1})$
  5.2. $t_n \leftarrow \text{argmax}\left(p(t_{d1,min}:)_{d2}\right) + t_{d1,min}$
6. **Return**: (t_p, t_i, t_n)

2.6. Hemodynamic analyses

Pressure waveforms captured with a brachial cuff system are in non-physiological units, as they represent the pressure fluctuations inside the cuff. To convert these waveforms into physiological units, we applied a previously validated calibration procedure using the blood pressure values from the oscillometric measurement [21]. The waveforms were scaled such that the peak pressure corresponds to SBP, and the base pressure corresponds to diastolic blood pressure (DBP). The calibration equation used is:

$$p_{calib} = \frac{p(t) - \min(p(t))}{\max(p(t)) - \min(p(t))} * (SBP - DBP) + DBP \tag{5}$$

where p_{calib} represents the calibrated pressure waveform.

Pulse wave analysis (PWA) was performed on the calibrated waveform to extract clinically significant parameters, including AIx, systolic pressure time integral (SPTI), and end-systolic pressure (ESP). These parameters were computed using both the measured (human-annotated) and PulseAI-generated fiducial points. Additionally, PTT—the foot-to-foot time difference between the start of the waveform at the central site (captured via catheter) and cuff waveforms—was calculated in milliseconds. PTT was further adjusted for subject height to derive a surrogate measure of PWV, herein denoted as sPWV, both of which serve as indicators of arterial stiffness [8].

$$AIx = \begin{cases} \dfrac{p(t_p) - p(t_i)}{p(t_p) - p(t_0)}, if\, t_i < t_p \\ \dfrac{p(t_i) - p(t_p)}{p(t_p) - p(t_0)}, otherwise \end{cases} \tag{6}$$

$$SPTI = \int_{t_0}^{t_n} p(t)dt \tag{7}$$

$$ESP = p(t_n) \tag{8}$$

$$PTT = t_{foot,cath} - t_{foot,cuff} \tag{9}$$

$$sPWV = \frac{Height}{PTT} \tag{10}$$

2.7. Statistical analyses

Fiducial point prediction accuracy was evaluated in the time domain. To recover the predicted fiducial point values, the unit-normalized predictions were multiplied by the cardiac cycle duration and rounded to the nearest millisecond (ms). Model performance was assessed by calculating the prediction error (true – predicted) for individual fiducial points, as well as the MAE for joint predictions. Several metrics were used to evaluate model accuracy, including the Pearson correlation coefficient (r), coefficient of determination (R^2), root mean squared error (RMSE), mean difference, and limits of agreement. The prediction accuracy for fiducial points and PWA-derived parameters was visualized using scatter plots of true-versus-predicted values and Bland-Altman analysis. Correlation strength was quantified using r and the intraclass correlation coefficient (ICC), along with 95% confidence intervals (95% CI). Bland-Altman analysis was also used to assess bias and limits of agreement. Significance level was set at a value of $p < 0.05$.

3. Results

3.1. Model development

The PulseAI model was trained on the training cohort (3,646 cardiac cycles) with an early stopping criterion based on the validation cohort (515 cardiac cycles) and evaluated on the testing cohort (1,054 cardiac cycles). Model architecture optimization, summarized in Fig. 2 and Table S3, was performed across four different model configurations and the empirical method. The mcCNN model demonstrated the highest fiducial point prediction accuracy, with a median [IQR] error (true − predicted) of 0 [-7, 7.75] ms for t_i and 1 [-3, 4] ms for t_n. The fNN model had the second-best performance, with a median [IQR] error of −3 [-17, 13] ms for t_i and −1 [-7, 6] ms for t_n. The combined MAE for fiducial point prediction was lowest for the mcCNN model (median [IQR] = 6 [3, 12.5] ms) and highest for the empirical method (median [IQR] = 73 [56, 96.5] ms). Both the mcCNN and fNN models significantly outperformed the other models in predicting t_i and t_n as measured with r and R^2, as shown in Table S2. The algorithms were tested with cross-validation on incremental relative training sizes, the fNN and mcCNN significantly outperformed the other models across all training sizes (Fig. S4). Based on these results, the mcCNN architecture was selected for further tuning.

Hyperparameter tuning was performed sequentially to explore potential improvements in model performance. Three sets of experiments were conducted to evaluate the loss function (experiments #1–3), data augmentation strategies (experiments #4–6), and regularization methods (experiments #7–9). The first set of experiments (#1–3) indicated that the MAE base loss function produced the most accurate predictions for t_i ($r = 0.88$, $R^2 = 0.77$, RMSE = 25 ms) and t_n ($r = 0.91$, $R^2 = 0.82$, RMSE = 17 ms), leading to its selection for subsequent experiments. The second set (#4–6) tested different data augmentation techniques. The truncate and resample method (experiment #4) yielded the best improvement for t_i prediction ($r = 0.92$, $R^2 = 0.85$, RMSE = 21 ms), while the combination of truncation and resampling, and scaling (experiment #6) provided the highest accuracy for t_n ($r = 0.94$, $R^2 = 0.88$, RMSE = 14 ms). Since the performance difference between experiments #4 and #6 for t_i was minimal, the configuration from experiment #6 was chosen for further testing. Finally, experiments #7–9 assessed different regularization techniques, but none resulted in improved prediction accuracy. A summary of the hyperparameter tuning results is provided in Table 2 and Fig. S5 in the supplementary material. Based on these findings, the final model configuration was selected from experiment #6. This corresponds to the mcCNN architecture with an MAE base loss function and data augmentation using both the truncate and resample method along with scaling. Specifically, the mcCNN model takes three channels as inputs – waveform, first and second derivative – and has three convolutional blocks followed by fully connected layers. The convolutional blocks are each made up of a 1D convolutional layer, a ReLU activation and a max pooling step; convolutional layers have 8, 16, and 16 dimensions, a kernel size of 3, and a stride and padding of 1. The fully connected layers convert feature maps to the fiducial point indices; the first layer is a dense layer with 128 units and ReLU activation and the output layer has 2 units.

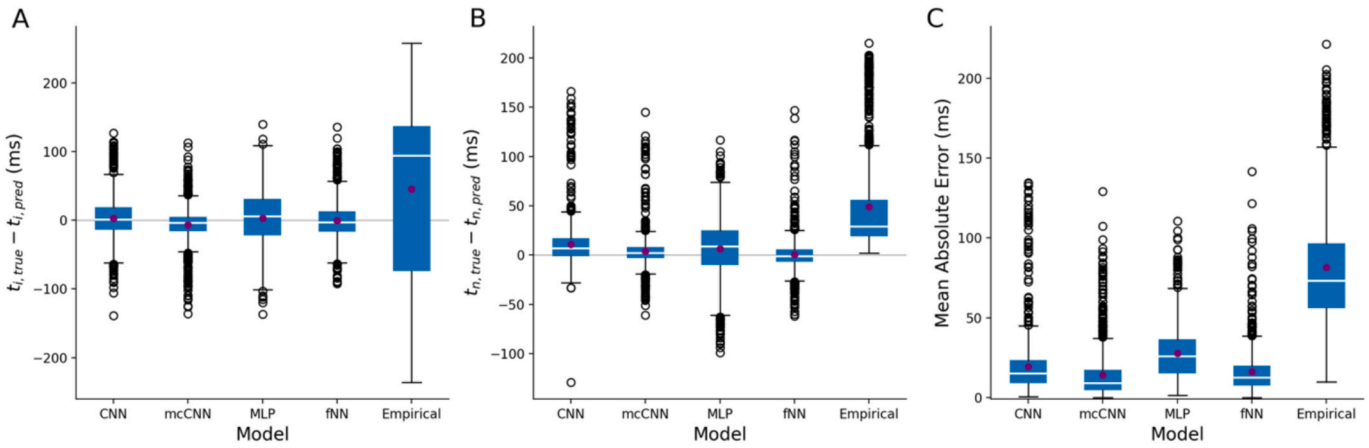

Fig. 2. Fiducial point prediction errors across different model architectures. (A) and (B) show the prediction error (true – predicted) for the inflection point, t_i, and the dicrotic notch, t_n, respectively. (C) Displays the mean absolute error (MAE) for fiducial point detection across various algorithms, including the convolutional neural network (CNN), multi-channel CNN (mcCNN), multi-layer perceptron (MLP), Fourier-based neural network (fNN), and the empirical model.

Table 2
Prediction accuracy metrics for the cardiac wave fiducial point predictions for the hyperparameter and algorithm tuning experiments.

		Experiment Number								
	Metric	1	2	3	4	5	6	7	8	9
t_i	**r**	0.85	0.88	0.86	0.92	0.86	0.91	0.89	0.91	0.89
	R^2	0.71	0.77	0.74	0.85	0.74	0.83	0.79	0.82	0.79
	RMSE, ms	29	25	27	21	27	22	24	22	24
	Mean Difference, ms	−7	−2	2	0	2	0	0	−1	−2
	Limits of Agreement, ms	54	49	53	41	52	42	47	44	47
t_n	**r**	0.89	0.91	0.90	0.89	0.91	0.94	0.92	0.92	0.89
	R^2	0.77	0.82	0.78	0.78	0.81	0.88	0.85	0.83	0.76
	RMSE, ms	19	17	18	18	17	14	15	16	19
	Mean Difference, ms	4	3	6	1	2	0	1	0	3
	Limits of Agreement, ms	37	32	34	36	33	27	30	32	37

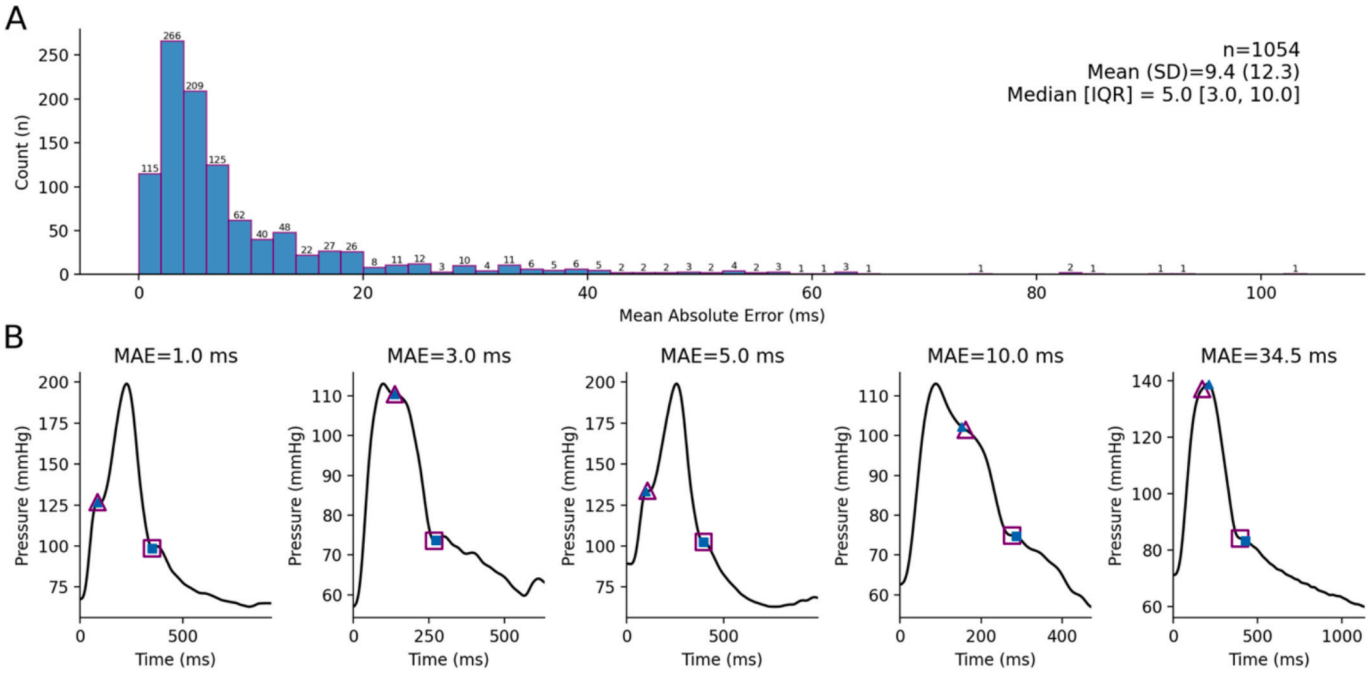

Fig. 3. Performance of the optimized PulseAI model error in the test population. (A) Mean absolute error (MAE) distribution across the test population (n = 1,054). (B) Five sample waveforms illustrating fiducial point predictions across the error spectrum at the 5th, 25th, 50th, 75th and 95th percentile of MAE.

3.2. Model evaluation

The PulseAI model, incorporating the mcCNN architecture, MAE loss function, and selected data augmentation strategies, was evaluated on the test cohort (1,054 cardiac cycles). Fig. 3A presents the model's MAE distribution, with a median [IQR] error of 5 [3,10] ms. Fig. 3B visualizes the positioning of true versus predicted fiducial points (t_i and t_n) across the entire error spectrum. The model reported an average MAE of 9.4 ms with a 95% confidence interval of [8.6, 10.1] and an average RMSE of 18.1 ms with a confidence interval of [17.3, 19.0]. Fig. 4 illustrates the prediction accuracy for fiducial points using true-versus-predicted plots and Bland-Altman analysis. The t_i point demonstrated a strong linear correlation ($r = 0.913$, $p < 0.0001$; ICC = 0.951) with no bias (B [LOA] = 0 [-42, 43] ms). Similarly, the t_n point exhibited a strong linear correlation ($r = 0.939$, $p < 0.0001$; ICC = 0.958), with no observed bias (B [LOA] = 0 [-27, 27] ms). The average error in fiducial point identification was below the permitted error range of 30 ms for both t_i (12.6 ms) and t_n (6.2 ms). A stratified analysis of the PulseAI model performance with the mcCNN architecture was performed for age, gender, and hypertensive status, results summarized in Table S4. Fig. 5 qualitatively demonstrates that prediction accuracy is consistent across the three pressure waveform types—Type A, Type B, and Type C—classified based on AIx.

3.3. Physiological relevancy of the approach

The true and predicted fiducial points were used to extract clinically relevant features from the cardiac pressure waveform via PWA. Fig. 6 compares PWA accuracy using PulseAI-predicted fiducial points versus true measurements (human-annotated) for AIx, SPTI, and ESP. AIx exhibited a strong correlation between predicted and true values ($r = 0.990$, $p < 0.0001$; ICC = 0.995) with no detectable bias (B [LOA] = 0 [-9, 8] %). Similarly, SPTI demonstrated high agreement ($r = 0.988$, $p < 0.0001$; ICC = 0.994) with negligible bias (B [LOA] = 0.0 [-2.1, 2.1] %). ESP also showed excellent concordance ($r = 0.998$, $p < 0.001$; ICC = 0.999) and minimal bias (B [LOA] = -0.2 [-1.4, 1.1] mmHg).

AIx values, computed using both true and predicted fiducial points, were further analyzed in relation to arterial stiffness metrics, specifically PTT (in milliseconds) and sPWV (in meters per second) (Fig. 7). Three instances with non-physiological negative PTT values were excluded. A tertile analysis of PTT classified the population into three subgroups: T1 (n = 362) with (8, 56] ms, T2 (n = 368) with (56, 66] ms, and T3 (n = 321) with (66, 85] ms. AIx demonstrated a clear inverse relationship with PTT, with significant differences observed between all tertiles (T1 vs. T2, T2 vs. T3, and T1 vs. T3; all $p < 0.05$). Additionally, no significant differences were found between true and predicted AIx values within each tertile group (all $p > 0.05$).

A similar tertile analysis was conducted for sPWV, dividing the population into T1 (n = 351) with (19, 25.5] m/s, T2 (n = 362) with (25.5, 30] m/s, and T3 (n = 338) with (30, 210] m/s. AIx exhibited a

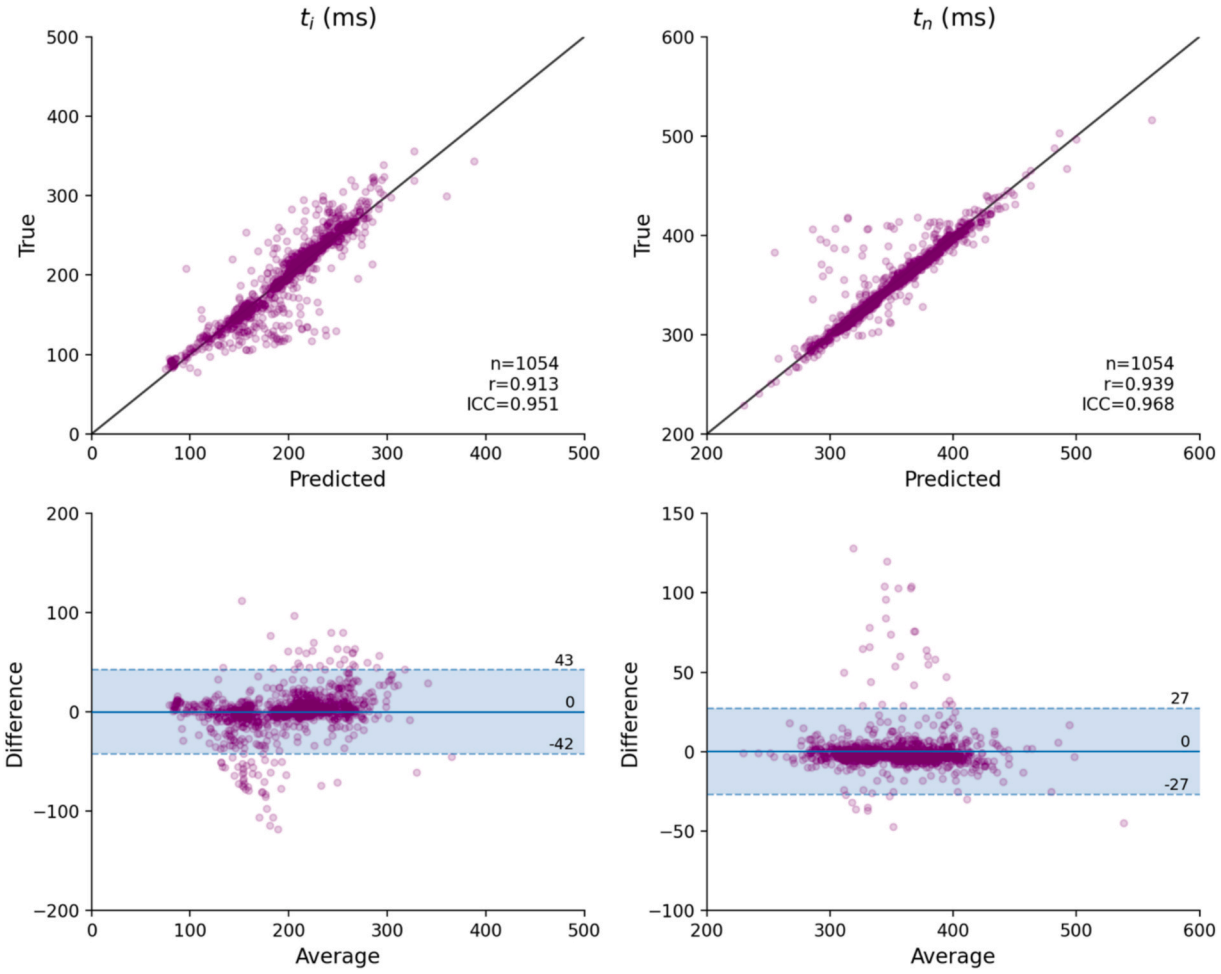

Fig. 4. Prediction accuracy of PulseAI for pulse waveform fiducial points. (Top) True-versus-predicted plots for fiducial points t_i and t_n, with the black solid line representing the line of proportionality. (Bottom) Bland-Altman plots for t_i and t_n where the solid blue line indicates the mean difference, and the shaded area represents the limits of agreement.

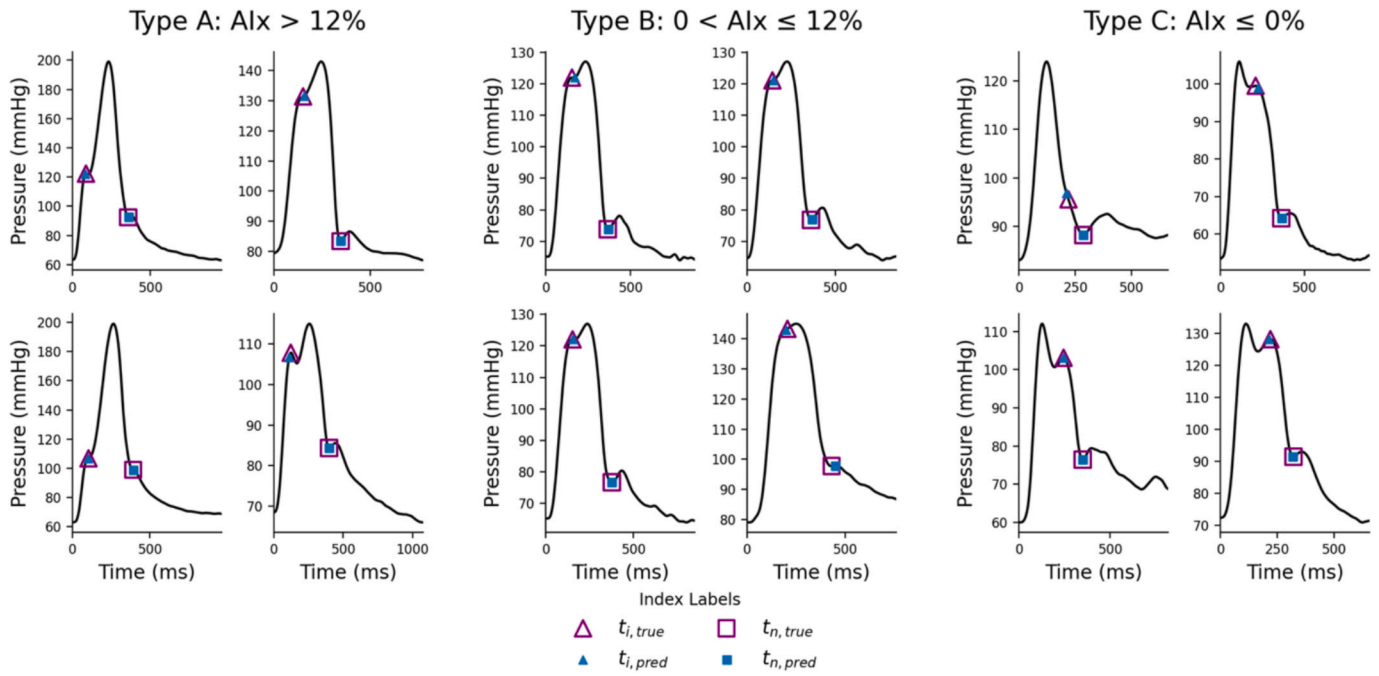

Fig. 5. PulseAI fiducial point predictions versus true measurement across different wave morphologies. True and predicted fiducial points are shown for waveforms classified based on the shape type according to Augmentation Index (AIx) morphology definitions.

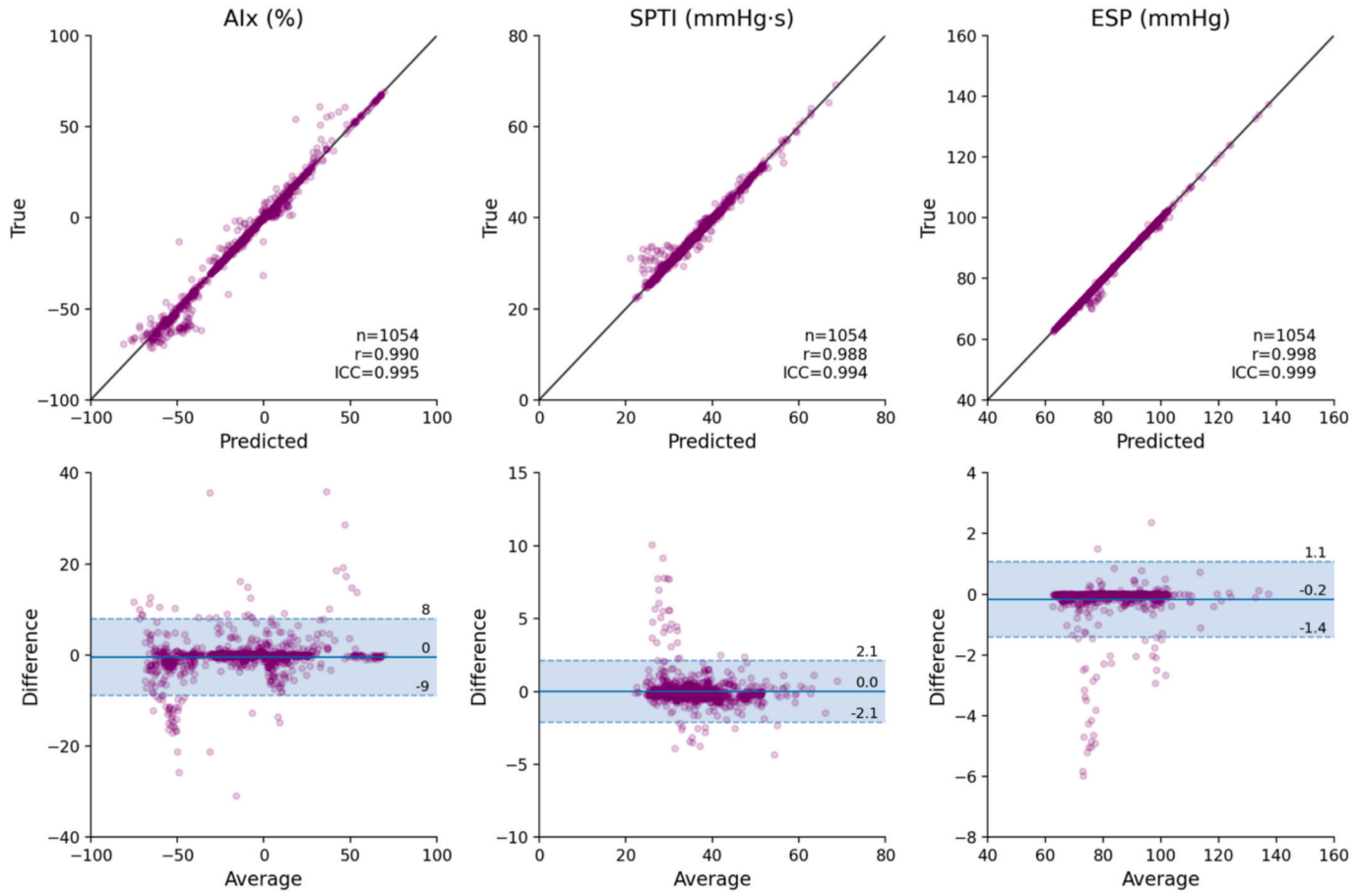

Fig. 6. Evaluation of pulse waveform analysis (PWA) accuracy using PulseAI-predicted fiducial points. (Top) True-versus-predicted plots for pulse waveform features extracted via PWA using true and predicted fiducial points. From left to right, the features include Augmentation Index (AIx), systolic pressure–time integral (SPTI), and end-systolic pressure (ESP). The black solid line represents the proportionality line. (Bottom) Bland-Altman plots for the PWA features, with the solid blue line denoting the mean difference, and the shaded area representing the limits of agreement.

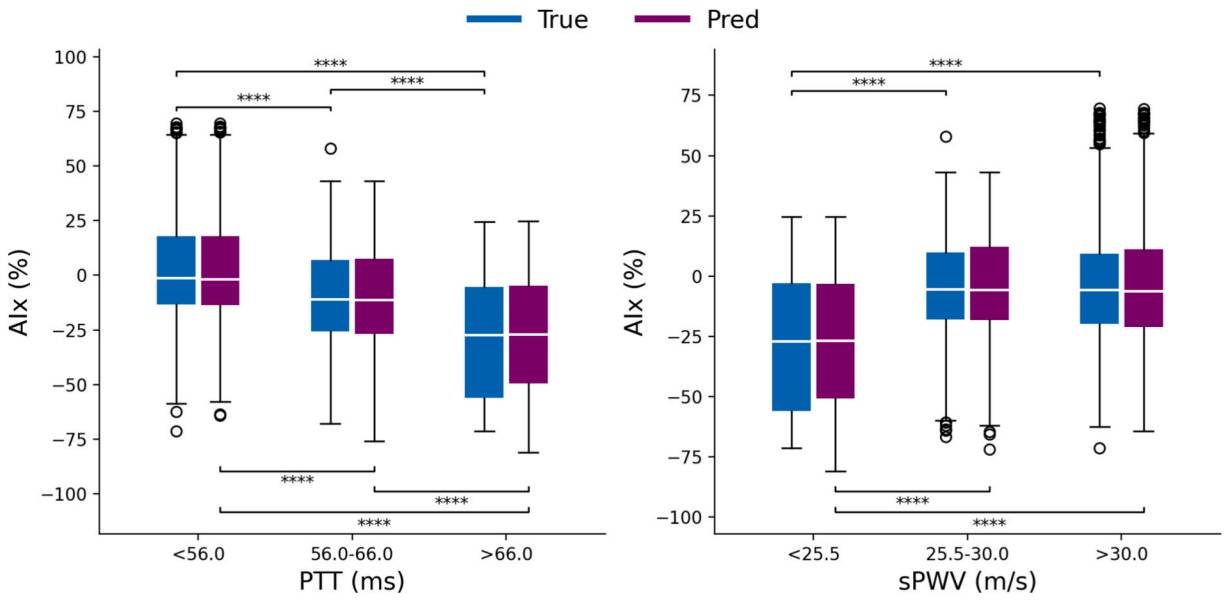

Fig. 7. Relationship between arterial stiffness and PulseAI-derived Augmentation Index (AIx). AIx measurements are compared with pulse transit time (PTT) and surrogate of pulse wave velocity (sPWV) as indirect measures of arterial stiffness. Statistical significance is marked as * $p < 0.05$, ** $p < 0.01$, *** $p < 0.001$, **** $p < 0.0001$.

positive correlation with sPWV, with significant differences found between T1 and T2 as well as between T1 and T3 (both $p < 0.05$), though no statistical difference was observed between T2 and T3 ($p > 0.05$). Also, for sPWV no significant differences were detected between true and predicted AIx values across all tertile groups (all $p > 0.05$).

4. Discussion

Consistent and reliable identification of fiducial points in a cardiac waveform is essential for accurate PWA, making this precursor step crucial in clinical assessments [38]. While certain fiducial points, such as the peak systolic pressure, are easily identifiable due to their distinct characteristics, others – like the dicrotic notch and the inflection point – are more challenging to define. This challenge is further amplified in noninvasive signals, where high-frequency components tend to be attenuated, making these features less distinct. In the literature, there are several mathematical definitions used for the identification of these points [36,39]. For example, Takazawa et al. used a conditional definition based on the fourth-order pressure derivative to determine whether the inflection point occurs before or after the systolic peak, followed by zero crossings to determine its precise location [35]. Other studies have used second order derivative crossings [37], while others have identified this point based on the intersection of tangents drawn at local minima and maxima in the waveform's first derivative [27]. Similar trends can be observed for the identification of the dicrotic notch. While the notch is easily defined when distinctly visible, its definition can become ambiguous in cases where it is represented by an incisura, making its identification reliant on higher-order derivative behaviors [34,40–43]. Moreover, the diversity in waveform morphologies may necessitate different identification strategies to ensure accurate detection across various patient populations and physiological conditions. Although these features are often easily identifiable by visual inspection from a trained individual, translating their characteristics into precise mathematical definitions is a complex task. This inherent complexity makes fiducial point detection particularly well-suited for machine learning-based pattern recognition approaches, which can effectively capture subtle waveform variations and improve detection robustness.

In this study, we evaluated multiple model architectures and preprocessing strategies to identify the optimal approach for fiducial point detection. Among the four tested architectures, the mcCNN demonstrated the lowest prediction error. This model processes the pressure signal along with its first and second derivatives to identify fiducial points, significantly outperforming the single-channel CNN model in terms of MAE ($p < 0.05$). This improvement suggests that incorporating the pressure signal's derivatives provided additional valuable information for the pattern recognition task. Interestingly, this result aligns with empirical strategies commonly described in the literature, where higher-order derivatives are employed to identify these fiducial points as signal characteristics are more apparent [35,37]. Given that the CNN architecture relies on filters to extract signal patterns, this additional information from the waveform derivatives appears to enhance model performance effectively.

As part of the model comparison, we also assessed the performance of an empirical method based on conventional definitions of fiducial points found in the literature [34,35]. As shown in Fig. 2 and Table S3 in the supplementary material, the machine learning models strongly outperformed the empirical method. The prediction of the inflection point, t_i, exhibited a wide error distribution, with interquartile ranges between −74 to 137 ms. This suggests that the empirical method frequently misidentified early systolic peaks as late systolic peaks, or vice versa, highlighting the difficulty in defining mathematical rules to classify such points. Another notable observation from this analysis is that the fNN method achieved only slightly lower performance than the mcCNN (mcCNN MAE = 6 ms; fNN MAE = 12.5 ms), while maintaining a substantially smaller model size (mcCNN = 257 k parameters; fNN = 15.5 K parameters). Although the mcCNN model was chosen for downstream analysis due to superior performance, these results highlight the effectiveness of spectral machine learning in developing compact yet accurate models [15,44,45].

Our findings further demonstrated that preprocessing strategies applied to the mcCNN model improved performance. The most notable improvement resulted from the data augmentation strategy, which involved modifying the input data such that a single data point was used multiple times in the training set with different configurations. The base dataset preprocessing included normalizing all input waveforms to a uniform length of 1000 units and standardizing the amplitude to have zero mean and unit standard deviation. Two data augmentation strategies were then applied: (1) rescaling the waveform amplitudes and (2) truncating and resampling the waveforms. Since the inflection point and

dicrotic notch follow physiological phenomena, they tend to occur in relatively consistent locations. Truncating and resampling shifted the location of these fiducial points within the waveform while preserving its key features. This strategy aimed to prevent the model from learning a fixed positional bias and instead focus on recognizing signal-based characteristics. Similarly, rescaling the waveform amplitude was designed to prevent the model from relying on amplitude patterns and instead promote recognition of relevant waveform features. Conceptually, these data augmentation strategies were intended to expand the effective size of the training dataset by allowing a single real data point to contribute multiple useful and non-redundant samples. This is particularly important in clinical data applications, where data collection is often challenging and time-consuming. By engineering effective augmentation techniques, we can maximize the utility of available data and improve model robustness in real-world scenarios.

The variability in waveform morphology is highly prevalent in noninvasive datasets, making it crucial for the model to generalize across the entire spectrum. To assess this, we first examined how prediction errors translated to the physical placement of fiducial points. As shown in Fig. 3B, across the MAE spectrum—from the 5th percentile to the 95th percentile—the placement of fiducial points remained well-preserved. We further investigated how the model's predictions varied with waveform morphology, measured using the AIx as defined by Murgo et al. [46]. As shown in Fig. 5, the model accurately identified fiducial points across the full spectrum of waveform morphologies—Type A, B, and C—correctly distinguishing early and late systolic peaks and appropriately placing the dicrotic notch, whether represented by a distinct notch or an incisura. These results demonstrate the model's strong generalizability to waveforms with diverse morphologies, which are commonly encountered in clinical measurements.

Accurate fiducial point detection is crucial for consistent PWA. While our detection method introduces minimal error (MAE = 5 ms), the error is sufficiently small to ensure a strong one-to-one correlation between waveform parameters measured using predicted fiducial points and those measured with human-annotated points (AIx $R^2 = 0.980$; SPTI $R^2 = 0.975$; ESP $R^2 = 0.998$). This level of precision is particularly important, as PWA is widely getting popular in both research and clinical settings to extract valuable information from pressure waveforms and aid in diagnostic assessments [16,47–50]. Arterial stiffness is an established independent predictor of adverse cardiovascular events and PWA is a key method for assessing this parameter [51–54]. AIx is closely linked to arterial properties, particularly through variations in pulse wave velocity and wave arrival time. As arterial stiffness increases, the pulse wave travels faster, causing the reflected wave from peripheral sites to return earlier during systole [55]. This premature arrival amplifies systolic pressure, thereby increasing left ventricular afterload [55]. In this study, we demonstrated the inverse relationship between AIx and PTT – the time of pressure wave propagation between two points along the arterial system [56]. Additionally, our findings demonstrate that a longer transit time reduces the reflected wave contribution to afterload, as measured by lower AIx values. Given that AIx is highly dependent on the precise and consistent identification of the waveform's inflection point [57], our results further highlight the critical role of accurate fiducial point detection for ensuring reliable PWA measurements. Therefore, we envision that PulseAI could be directly integrated into PWA of cardiac pressure waveform to perform single-site monitoring of arterial stiffness via AIx.

This study and its models have some limitations. First, the models were trained only on waveforms from a brachial cuff system in sSBP hold. Since pressure waveform morphology varies throughout the arterial tree, these models may not perform optimally on waveforms from different measurement sites or modalities. Expanding the training dataset to include diverse waveform sources is essential for broader applicability. Another limitation is the trade-off between generalizability and accuracy. While our ML model effectively handles diverse waveform morphologies, this flexibility may reduce precision in highly consistent waveform patterns. In such cases, empirical methods may outperform the model, as they can achieve near-perfect accuracy when waveform characteristics are stable and well-defined. However, in real-world clinical data, where waveform variability is common, our model's adaptability is key to ensuring reliable performance across different patient profiles and conditions. Lastly, we acknowledge the ongoing debate in the literature regarding the use of AIx to assess arterial stiffness. At the level of wave dynamics, AIx is governed by arterial wave reflections and vascular properties, however several physiological factors strongly modulate this relationship. As such, some studies have reported weak or inconsistent associations between AIx and arterial stiffness [58–60]. While this study is motivated by the clinical relevance of AIx, we recognize that AIx might not always serve as a standalone assessment of arterial stiffness.

5. Conclusion

Our study developed and validated the PulseAI method for identifying t_i and t_n on a cardiac waveform to serve as a tool for monitoring arterial stiffness from single-site pressure measurements. PulseAI was trained to predict the location of fiducial points from resampled and standardized pressure waveforms measured using a brachial cuff in the sSBP hold. The optimized model demonstrated strong predictive accuracy, achieving a MAE of 9.4 ms overall, with errors of 12.6 ms for t_i and of 6.2 ms for t_n, both of which fall within the acceptance error range of 30 ms. Accurate fiducial point detection is the foundation for reliable PWA, which enabled precise measurements of AIx, SPTI, and ESP using the predicted fiducial points. AIx from the brachial waveform revealed an inverse relationship with PTT, a surrogate metric of PWV, consistent with established arterial stiffness metrics. These results highlighted that AIx measured at the brachial is sensitive to elevated arterial stiffness. In conclusion, this study demonstrated that machine learning-based fiducial point detection provides a reliable approach for accurate PWA and a practical tool for single-site assessment of arterial stiffness-related metrics.

6. Declaration of generative AI and AI-assisted technologies in the manuscript preparation process

During the preparation of this work the author(s) used ChatGPT for proofreading and editing purposes. After using this tool/service, the author(s) reviewed and edited the content as needed and take(s) full responsibility for the scientific content and accuracy of the published article.

CRediT authorship contribution statement

Alessio Tamborini: Writing – review & editing, Writing – original draft, Visualization, Validation, Software, Methodology, Investigation, Formal analysis, Data curation, Conceptualization. **Arian Aghilinejad:** Writing – review & editing, Supervision, Methodology, Conceptualization. **Morteza Gharib:** Writing – review & editing, Supervision, Methodology, Investigation, Conceptualization.

Declaration of competing interest

The authors declare that they have no known competing financial interests or personal relationships that could have appeared to influence the work reported in this paper.

Acknowledgements

Part of figure 1 and the Graphical Abstract were generated with adapted illustrations from Servier Medical Art, provided by Servier and licensed under a Creative Commons Attribution 3.0 Unported License.

Appendix A. Supplementary data

Supplementary data to this article can be found online at https://doi.org/10.1016/j.bspc.2026.109840.

Data availability

The authors do not have permission to share data.

References

[1] S. S. Martin *et al.*, "2024 Heart Disease and Stroke Statistics: A Report of US and Global Data From the American Heart Association," *Circulation*, vol. 149, no. 8, Feb. 2024, doi: 10.1161/CIR.0000000000001209.

[2] S. Laurent, et al., Aortic stiffness is an independent predictor of all-cause and cardiovascular mortality in hypertensive patients, Hypertension 37 (5) (May 2001) 1236–1241, https://doi.org/10.1161/01.HYP.37.5.1236.

[3] J. He, P.K. Whelton, Elevated systolic blood pressure and risk of cardiovascular and renal disease: overview of evidence from observational epidemiologic studies and randomized controlled trials, Am. Heart J. 138 (3 Pt 2) (Sep. 1999) 211–219, https://doi.org/10.1016/s0002-8703(99)70312-1.

[4] K. Sutton-Tyrrell, et al., Elevated aortic pulse wave velocity, a marker of arterial stiffness, predicts cardiovascular events in well-functioning older adults, Circulation 111 (25) (Jun. 2005) 3384–3390, https://doi.org/10.1161/CIRCULATIONAHA.104.483628.

[5] P. Boutouyrie, P. Chowienczyk, J.D. Humphrey, G.F. Mitchell, Arterial stiffness and cardiovascular risk in hypertension, Circ. Res. 128 (7) (Apr. 2021) 864–886, https://doi.org/10.1161/CIRCRESAHA.121.318061.

[6] G.F. Mitchell, et al., Arterial stiffness and cardiovascular events, Circulation 121 (4) (Feb. 2010) 505–511, https://doi.org/10.1161/CIRCULATIONAHA.109.886655.

[7] J.P. Merillon, G. Motte, J. Fruchaud, C. Masquet, R. Gourgon, Evaluation of the elasticity and characteristic impedance of the ascending aorta in man, Cardiovasc. Res. 12 (7) (Jul. 1978) 401–406, https://doi.org/10.1093/cvr/12.7.401.

[8] R. Asmar, et al., Assessment of arterial distensibility by automatic pulse wave velocity measurement, Hypertension 26 (3) (Sep. 1995) 485–490, https://doi.org/10.1161/01.HYP.26.3.485.

[9] I.B. Wilkinson, K.M. Mäki-Petäjä, G.F. Mitchell, Uses of arterial stiffness in clinical practice, Arterioscler. Thromb. Vasc. Biol. 40 (5) (May 2020) 1063–1067, https://doi.org/10.1161/ATVBAHA.120.313130.

[10] W. Jin, P. Chowienczyk, J. Alastruey, Estimating pulse wave velocity from the radial pressure wave using machine learning algorithms, PLoS One 16 (6) (Jun. 2021) e0245026, https://doi.org/10.1371/journal.pone.0245026.

[11] G.F. Mitchell, et al., Vascular age assessed from an uncalibrated, noninvasive pressure waveform by using a deep learning approach: the AI-vascularAge model, Hypertension 81 (1) (Jan. 2024) 193–201, https://doi.org/10.1161/HYPERTENSIONAHA.123.21638.

[12] S. J. Al'Aref *et al.*, "Clinical applications of machine learning in cardiovascular disease and its relevance to cardiac imaging," *Eur Heart J*, vol. 40, no. 24, pp. 1975–1986, Jun. 2019, doi: 10.1093/eurheartj/ehy404.

[13] C. Krittanawong, et al., Machine learning prediction in cardiovascular diseases: a meta-analysis, Sci. Rep. 10 (1) (Sep. 2020) 16057, https://doi.org/10.1038/s41598-020-72685-1.

[14] A. Tamborini, A. Aghilinejad, R. V. Matthews, and M. Gharib, "Machine Learning Reconstruction of Left Ventricular Pressure From Peripheral Waveforms," *JACC: Advances*, vol. 4, no. 9, p. 102104, Sep. 2025, doi: 10.1016/j.jacadv.2025.102104.

[15] A. Tamborini, A. Aghilinejad, M. Gharib, A spectral machine learning approach to derive central aortic pressure waveforms from a brachial cuff, Proc. Natl. Acad. Sci. U.S.A. 122 (9) (Mar. 2025) e2416006122, https://doi.org/10.1073/pnas.2416006122.

[16] I.B. Wilkinson, H. MacCallum, L. Flint, J.R. Cockcroft, D.E. Newby, D.J. Webb, The influence of heart rate on augmentation index and central arterial pressure in humans, J. Physiol. 525 (Pt 1) (May 2000) 263–270, https://doi.org/10.1111/j.1469-7793.2000.t01-1-00263.x.

[17] C.-H. Chen, et al., Estimation of central aortic pressure waveform by mathematical transformation of radial tonometry pressure, Circulation 95 (7) (Apr. 1997) 1827–1836, https://doi.org/10.1161/01.CIR.95.7.1827.

[18] J.E. Sharman, J.E. Davies, C. Jenkins, T.H. Marwick, Augmentation index, left ventricular contractility, and wave reflection, Hypertension 54 (5) (Nov. 2009) 1099–1105, https://doi.org/10.1161/HYPERTENSIONAHA.109.133066.

[19] B.T. Costello, M.G. Schultz, J.A. Black, J.E. Sharman, Evaluation of a brachial cuff and suprasystolic waveform algorithm method to noninvasively derive central blood pressure, Am. J. Hypertens. 28 (4) (Apr. 2015) 480–486, https://doi.org/10.1093/ajh/hpu163.

[20] T. Weber, et al., Validation of a brachial cuff-based method for estimating central systolic blood pressure, Hypertension 58 (5) (Nov. 2011) 825–832, https://doi.org/10.1161/HYPERTENSIONAHA.111.176313.

[21] A. Tamborini, M. Gharib, Validation of a suprasystolic cuff system for static and dynamic representation of the central pressure waveform, J. Am. Heart Assoc. 13 (8) (Apr. 2024) e033290, https://doi.org/10.1161/JAHA.123.033290.

[22] A. Lowe, W. Harrison, E. El-Aklouk, P. Ruygrok, A.M. Al-Jumaily, Non-invasive model-based estimation of aortic pulse pressure using suprasystolic brachial pressure waveforms, J. Biomech. 42 (13) (Sep. 2009) 2111–2115, https://doi.org/10.1016/j.jbiomech.2009.05.029.

[23] V. Fabian *et al.*, "Noninvasive Assessment of Aortic Pulse Wave Velocity by the Brachial Occlusion-Cuff Technique: Comparative Study," *Sensors*, vol. 19, no. 16, Art. no. 16, Jan. 2019, doi: 10.3390/s19163467.

[24] A. Tamborini, M. Gharib, Listening to heart sounds through the pressure waveform, Sci. Rep. 14 (2024) 26824. https://doi.org/10.1038/s41598-024-78554-5.

[25] J. Sugawara, et al., Brachial–ankle pulse wave velocity: an index of central arterial stiffness? J. Hum. Hypertens. 19 (5) (May 2005) 401–406, https://doi.org/10.1038/sj.jhh.1001838.

[26] J. Sugawara, K. Hayashi, H. Tanaka, Distal shift of arterial pressure wave reflection sites with aging, Hypertension 56 (5) (Nov. 2010) 920–925, https://doi.org/10.1161/HYPERTENSIONAHA.110.160549.

[27] S. Munir, et al., Peripheral augmentation index defines the relationship between central and peripheral pulse pressure, Hypertension 51 (1) (Jan. 2008) 112–118, https://doi.org/10.1161/HYPERTENSIONAHA.107.096016.

[28] H. Ueda, Y. Nakayama, K. Tsumura, K. Yoshimaru, T. Hayashi, J. Yoshikawa, Inflection point of ascending aortic waveform is a powerful predictor of restenosis after percutaneous transluminal coronary angioplasty*, Am. J. Hypertens. 15 (9) (Sep. 2002) 823–826, https://doi.org/10.1016/S0895-7061(02)02981-3.

[29] M. Saffarpour *et al.*, "Physiowise: A Physics-aware Approach to Dicrotic Notch Identification," *ACM Trans. Comput. Healthcare*, vol. 4, no. 2, p. 10:1-10:17, Apr. 2023, doi: 10.1145/3578556.

[30] R. Pal, A. Rudas, S. Kim, J.N. Chiang, A. Barney, M. Cannesson, An algorithm to detect dicrotic notch in arterial blood pressure and photoplethysmography waveforms using the iterative envelope mean method, Comput. Methods Programs Biomed. 254 (Sep. 2024) 108283, https://doi.org/10.1016/j.cmpb.2024.108283.

[31] R. Pal, A. Rudas, T. Williams, J. N. Chiang, A. Barney, and M. Cannesson, "Feature extraction tool using temporal landmarks in arterial blood pressure and photoplethysmography waveforms," *npj Cardiovasc Health*, vol. 2, no. 1, p. 57, Nov. 2025, doi: 10.1038/s44325-025-00096-0.

[32] S.A.A.P. Hoeksel, J.R.C. Jansen, J.A. Blom, J.J. Schreuder, Detection of dicrotic notch in arterial pressure signals, J. Clin. Monit. Comput. 13 (5) (Sep. 1997) 309–316, https://doi.org/10.1023/A:1007414906294.

[33] A. Tamborini, M. Gharib, A Pneumatic low-pass filter for high-fidelity cuff-based pulse waveform acquisition, Ann. Biomed. Eng. 51 (11) (Nov. 2023) 2617–2628, https://doi.org/10.1007/s10439-023-03312-z.

[34] P.S. Nandi, D.H. Spodick, Determination of systolic intervals utilizing the carotid first derivative, Am. Heart J. 86 (4) (Oct. 1973) 495–500, https://doi.org/10.1016/0002-8703(73)90141-5.

[35] K. Takazawa, N. Tanaka, K. Takeda, F. Kurosu, C. Ibukiyama, Underestimation of vasodilator effects of nitroglycerin by upper limb blood pressure, Hypertension 26 (3) (Sep. 1995) 520–523, https://doi.org/10.1161/01.HYP.26.3.520.

[36] L. Peter, J. Kracik, M. Cerny, N. Noury, and S. Polzer, "Mathematical Model Based on the Shape of Pulse Waves Measured at a Single Spot for the Non-Invasive Prediction of Blood Pressure," *Processes*, vol. 8, no. 4, Art. no. 4, Apr. 2020, doi: 10.3390/pr8040442.

[37] K. Takazawa, et al., Assessment of vasoactive agents and vascular aging by the second derivative of photoplethysmogram waveform, Hypertension 32 (2) (Aug. 1998) 365–370, https://doi.org/10.1161/01.HYP.32.2.365.

[38] M.Z. Suboh, R. Jaafar, N.A. Nayan, N.H. Harun, M.S.F. Mohamad, Analysis on four derivative waveforms of photoplethysmogram (PPG) for fiducial point detection, Front. Public Health 10 (Jun. 2022), https://doi.org/10.3389/fpubh.2022.920946.

[39] L.M. Van Bortel, et al., Non-invasive assessment of local arterial pulse pressure: comparison of applanation tonometry and echo-tracking, J. Hypertens. 19 (6) (Jun. 2001) 1037.

[40] M.C. Kyle, E.D. Freis, Computer identification of systolic time intervals, Comput. Biomed. Res. 3 (6) (Dec. 1970) 637–651, https://doi.org/10.1016/0010-4809(70)90031-5.

[41] R.H. Swatzell, W.H. Bancroft, J. Macy, E.E. Eddleman, The on-line computer system for determining the systolic time intervals, Comput. Biomed. Res. 6 (5) (Oct. 1973) 465–473, https://doi.org/10.1016/0010-4809(73)90079-7.

[42] M.J. Oppenheim, D.F. Sittig, An innovative dicrotic notch detection algorithm which combines rule-based logic with digital signal processing techniques, Comput. Biomed. Res. 28 (2) (Apr. 1995) 154–170, https://doi.org/10.1006/cbmr.1995.1011.

[43] L. Peter, N. Noury, M. Cerny, and I. Nykl, "Comparison of methods for the evaluation of NIBP from pulse transit time," in *2016 38th Annual International Conference of the IEEE Engineering in Medicine and Biology Society (EMBC)*, Aug. 2016, pp. 4244–4247. doi: 10.1109/EMBC.2016.7591664.

[44] A. Aghilinejad, A. Tamborini, and M. Gharib, "A new methodology for determining the central pressure waveform from peripheral measurement using Fourier-based machine learning," *Artificial Intelligence in Medicine*, p. 102918, Jun. 2024, doi: 10.1016/j.artmed.2024.102918.

[45] A. Aghilinejad and M. Gharib, "Assessing pressure wave components for aortic stiffness monitoring through spectral regression learning," *European Heart Journal Open*, vol. 4, no. 3, p. oeae040, May 2024, doi: 10.1093/ehjopen/oeae040.

[46] J.P. Murgo, N. Westerhof, J.P. Giolma, S.A. Altobelli, Aortic input impedance in normal man: relationship to pressure wave forms, Circulation 62 (1) (Jul. 1980) 105–116, https://doi.org/10.1161/01.CIR.62.1.105.

[47] M.F. O'Rourke, D.E. Gallagher, Pulse wave analysis, J. Hypertens. Suppl. 14 (5) (Dec. 1996) S147–S157.

[48] I.B. Wilkinson, et al., Reproducibility of pulse wave velocity and augmentation index measured by pulse wave analysis, J. Hypertens. 16 (12) (Dec. 1998) 2079.

[49] A. Tamborini, A. Aghilinejad, and M. Gharib, "Abstract 4141635: Reconstructing Invasive Aortic Pressure Waveforms from Non-Invasive Brachial Measurements

Using a Machine Learning Approach," *Circulation*, vol. 150, no. Suppl_1, pp. A4141635–A4141635, Nov. 2024, doi: 10.1161/circ.150.suppl_1.4141635.
[50] A. Aghilinejad, A. Tamborini, and M. Gharib, "Abstract 4142004: Predicting Cardiovascular Disease Events Using Uncalibrated Non-invasive Carotid Pressure Wave Components from Spectral Regression Learning," *Circulation*, vol. 150, no. Suppl_1, pp. A4142004–A4142004, Nov. 2024, doi: 10.1161/circ.150.suppl_1.4142004.
[51] W.W. Nichols, Clinical measurement of arterial stiffness obtained from noninvasive pressure waveforms, Am. J. Hypertens. 18 (S1) (Jan. 2005) 3S–10S, https://doi.org/10.1016/j.amjhyper.2004.10.009.
[52] J.J. Oliver, D.J. Webb, Noninvasive assessment of arterial stiffness and risk of atherosclerotic events, Arterioscler. Thromb. Vasc. Biol. 23 (4) (Apr. 2003) 554–566, https://doi.org/10.1161/01.ATV.0000060460.52916.D6.
[53] S. Meaume, A. Benetos, O.F. Henry, A. Rudnichi, M.E. Safar, Aortic pulse wave velocity predicts cardiovascular mortality in subjects >70 years of age, Arterioscler. Thromb. Vasc. Biol. 21 (12) (Dec. 2001) 2046–2050, https://doi.org/10.1161/hq1201.100226.
[54] A. Aghilinejad, A. Tamborini, and M. Gharib, "Decoding vascular age from brachial waveform morphology via machine learning and model-based data augmentation," *Mach. Learn.: Health*, vol. 1, no. 1, p. 015006, Dec. 2025, doi: 10.1088/3049-477X/adf74f.
[55] W.W. Nichols, D.G. Edwards, Arterial elastance and wave reflection augmentation of systolic blood pressure: deleterious effects and implications for therapy, J. Cardiovasc. Pharmacol. Ther. 6 (1) (Mar. 2001) 5–21, https://doi.org/10.1177/107424840100600102.
[56] Y.-L. Zhang, Y.-Y. Zheng, Z.-C. Ma, Y.-N. Sun, Radial pulse transit time is an index of arterial stiffness, Hypertens. Res. 34 (7) (Jul. 2011) 884–887, https://doi.org/10.1038/hr.2011.41.
[57] M.F. O'Rourke, A.L. Pauca, Augmentation of the aortic and central arterial pressure waveform, Blood Press. Monit. 9 (4) (Aug. 2004) 179.
[58] P.S. Lacy, D.G. O'Brien, A.G. Stanley, M.M. Dewar, P.P. Swales, B. Williams, Increased pulse wave velocity is not associated with elevated augmentation index in patients with diabetes, J. Hypertens. 22 (10) (Oct. 2004) 1937.
[59] A. Hughes, et al., Limitations of augmentation index in the assessment of wave reflection in normotensive healthy individuals, PLoS One 8 (Mar. 2013) e59371, https://doi.org/10.1371/journal.pone.0059371.
[60] F. Fantin, A. Mattocks, C.J. Bulpitt, W. Banya, C. Rajkumar, Is augmentation index a good measure of vascular stiffness in the elderly? Age Ageing 36 (1) (Jan. 2007) 43–48, https://doi.org/10.1093/ageing/afl115.